RSC Advances

ROYAL SOCIETY OF CHEMISTRY

www.rsc.org/advances

RSC Advances

ARTICLE

Excitation dependent recombination studies on SnO2/TiO2 electrospun nanofibers†

New
Received 16th July 2015,
Accepted 00th July 2015

DOI: 10.1039/x0xx00000x

www.rsc.org/

Veluru Jagadeesh babu[a,*], Sesha Vempati [a,*], Yelda Ertas[a], Tamer Uyar [a,b,*],

Poly (vinyl acetate; PVAc)/TiO_2 nanofibers, PVAc/SnO_2 nanoribbons and PVAc/SnO_2/TiO_2 nanoribbons were produced *via* electrospinning. TiO_2 nanofibers and SnO_2 nanoribbons were obtained by removal of polymeric matrix (PVAc) after the calcination at 450 °C, interestingly, PVAc/SnO_2-TiO_2nanoribbons were transformed into SnO_2-TiO_2 nanofibers after calcination at the same condition. The X-ray diffraction measurements suggested the presence of the anatase TiO_2, rutile SnO_2 and both were present in the SnO_2-TiO_2 mixed system. Systematic photoluminescence studies were performed on electrospun nanostructures at different excitation wavelengths (λ_{ex1}=325, λ_{ex2}=330, λ_{ex3}=350, λ_{ex4}=397 and λ_{ex5}=540 nm). We emphasize that the defect levels in the SnO_2-TiO_2 mixed system based on the defects in individual systems and anticipate that these defect levels may have great potential in understanding and characterizing various semiconducting nanostructures.

Introduction

1-D nanostructures *via* electrospinning have attracted significantly due to their distinctive surface and quantum effects can influence the functionality and performance in nanodevices [1-5]. Among the semiconductors SnO_2 and TiO_2 have evoked considerable attention due to their potential applications in optoelectronic devices [6-8], despite the anatase phase of TiO_2 is being more photoactive[9]. It has been found that the combination of SnO_2 and TiO_2 give most significant sensing and photocatalysis applications [10, 11]. In addition, SnO_2 and TiO_2 have large band gap (3.2 eV for anatase TiO_2 and 3.6 eV for the SnO_2) [12, 13] ensures the electrons within the conduction band (CB) have a strong reducing ability and holes in the valence band (VB) have strong oxidizing ability [14]. The impurities or defect states induced by the synthesis methods can form deep energy levels (act as trapping centres) or shallow energy levels (act as donors)[15]. These shallow trap levels (lying in the band gap) act as carrier traps in competition with the fast carrier recombination in the bulk during photoexcitation, which enhances the photoactivity of the nanostructures. On the other hand, Zhu et.al [16] reported by considering chemical potentials the deep trap levels exhibited the reduced photocatalytic activities. Titania is a highly ionic lattice [17] with VB composed of oxygen 2p orbitals (wave functions considerably localized on the O^{-2} lattice site), while the CB consists mostly of excited states of Ti^{+4}. The width of the VB in O^{-2} 2p is about 16 eV and the breadth of the CB in Ti^{+4} 3d is about 27 eV [18].

Optical spectroscopy studies have been used extensively for detection of the CB electrons, trapped electrons, holes, and transition energy levels. Ghosh et.al [14] reported that in the rutile TiO_2 single crystal consists of at least eight shallow trap levels (<1 eV below CB). Later, the midgap energy related defects were identified from surface or bulk trap state luminescence either by surface modification of TiO_2 nanoparticels with loading of platinum[19] or by treatment with $TiCl_4$[20]. Ariga et.al., [21] demonstrated that the photo-oxidation of format on the TiO_2 (001) surface has a threshold energy between 2.1 and 2.3 eV (539−590 nm), apparently much lower than that of the bandgap energy (3.0−3.2 eV). The two defect related bands were observed in titanate nanostructures (at 463 and 533 nm) [22] and assigned to carrier trapping at defect centers. On the other hand, the optical properties of SnO_2 are of great importance because of the even parity symmetry which precludes from the band-edge radiation transition[23]. Upon reducing dimensionality of the SnO_2 crystals, the wave function symmetry can be broken due to quantum confinement and hence the dipole forbidden selection rule can be relieved, giving rise to the free exciton emission [24]. The luminescence would be dependent on shape of nanostructures such as fishbone-like nanoribbons of SnO_2 exhibited green emission[25]. Luo et.al [26] performed the temperature dependent PL on the SnO_2 nanowires and nanobelts where two bands centered at 470 nm and 560 nm were observed with the intensity of the former band was strongly dependent on temperature. The blue/violet emission was also reported for different shapes of SnO_2 nanocauliflowers, nanoblades, and other type of nanostructures[27-30]. Kar et.al[31], reported that the morphology dependent luminescence for the SnO_2 nanorods and

[a.] UNAM-National Nanotechnology Research Centre, Bilkent University, Ankara, 06800, Turkey.
[b.] Institute of Materials Science& Nanotechnology, BIlkent University, Ankara, 06800, Turkey.
[c] Contact: vjbabu2002@gmail.com; svempati01@qub.ac.uk; uyar@unam.bilkent.edu.tr;
† Electronic Supplementary Information (ESI) available. See
DOI: 10.1039/x0xx00000x

nanoparticles. The exciton binding energy of SnO_2 is as large as 130 meV, which envisages efficient exciton emission at room temperature and even at higher temperatures. Kılıç and Zunger[32], observed five intrinsic defects coexistence in SnO_2 are oxygen vacancy (V_O s), tin vacancy (V_{sn}), tin antisite (Sn_O), oxygen interstitial (O_i) and tin interstitial (Sn_i). Sn_i and V_O are the predominant defect structures in SnO_2 due to multivalancy of tin. These defect structures can produce shallow donor levels cause to n-type conduction which is originating from the V_O s, where V_O s can capture electrons lead to singly ionized vacancies (V_O^+) or doubly ionized vacancies (V_O^{++}). However, there is an inadequate report on electrospun SnO_2/TiO_2 nanofibers with excitation dependent emission spectra analysis.

In the present study, we observe that the excitation dependent photoluminescence (PL) studies on SnO_2/TiO_2 electrospun nanofibers derived from that of nanoribbons of mixed system. The PL emission peaks for the SnO_2, TiO_2 and SnO_2/TiO_2 are dependent on the band gap and surface defects. The proposed band alignment is also discussed in terms of the excitation energy.

Experimental

Materials

Titanium (IV) isopropoxide (TIP, 97 %, Sigma-Aldrich); Tin (IV) Chloride ($SnCl_4$, 99%, Sigma-Aldrich); Poly (vinyl acetate Mw:350 000); Methanol (99%, Sigma-Aldrich); glacial acetic acid (100%, Merck). All the chemicals were used without further purification.

Synthesis of the nanostructures

The preparation of nanostructures *via* electrospinning is a well-known technology[33, 34]. The polymer solutions was prepared by dissolving 1.2 g of PVAc in 10 mL of methanol and stirred for ~3 h. For the TiO_2 preparation, 2 mL of glacial acetic acid was added to the polymer solution, followed by 1 mL TIP which was then subjected to stirring for ~6 h to obtain clear and homogeneous solution. For the SnO_2 synthesis, 0.5 mL of $SnCl_4$ was added to the polymer solution (PVAc) and subjected to stirring for ~6h. Whereas SnO_2-TiO_2 solution, 2 mL of glacial acetic acid, 1 mL TIP and 0.5 mL of $SnCl_4$ added to the polymer solution (PVAc) and subjected to the ~6h of stirring.

The solution was taken in a 10 mL syringe (21 G 1/2 needle) were placed in a commercially available electrospinning machine Nanoweb (Electrospin 100) for the preparation of nanofibers. The flow rate was adjusted to 25 μL/m with a syringe pump (KD Scientific, KDS 101), the distance between the two electrodes (tip of the needle to collector) was maintained at 8 cm, applied voltage between the rotating drum collector (with speed of 200 rpm) and the tip of the needle was 15 kV. The electrospun PVAc/TiO_2 nanofibers, SnO_2-nanoribbons and SnO_2- TiO_2 nanoribbons were then subjected to calcination at 450 °C for about 3h, after calcination the samples are referred in short form as TNF, SNR and STNF, respectively.

Characterization

The thermal analysis was performed on nanostructures using thermogravimetric analyser (TGA, Q500, TA Instruments) in the range of room temperature (T_R) to 700 °C in a nitrogen atmosphere. The morphologies of the microstructures and nanostructures were observed by scanning electron microscopy (SEM, FEI-Quanta 200 FEG). Approximately 5 nm of Au/Pd was sputtered on samples before subjected to the SEM scanning. Nanofibers were examined under transmission electron microscope (TEM, FEI-Tecnai G2 F30). The samples were dispersed in ethanol and a tiny drop was dried on holey carbon coated TEM grid and analysed with energy dispersive X-ray spectroscopy (EDX) for elemental analysis. The crystal structures of the nanofibers were characterized by using PANalytical X'Pert Pro multipurpose X-ray diffractometer (XRD) in the range of 2θ = 20-80° with CuKα (1.5418 Å) radiation. UV-vis absorbance spectroscopy of the nanostructures was performed using UV-vis spectrometer (VARIAN, Cary 5000) by taking nearly 1-5 mg of dispersion is taken in quartz curette. PL measurements were performed on the fibers as free standing flakes in the PL spectrometer (Jobin Yvon, FL-1057 TCSPC) at different excitation wavelengths (λ_{ex1} =325, λ_{ex2} =330, λ_{ex3} =350, λ_{ex4} =397 and λ_{ex5}= 540 nm). XRD peaks and PL emission peaks were deconvoluted with Lorentz and Gauss fitting resepectively, with Origin 8.5 where it necessary.

Results and Discussion

Surface morphology

The surface morphology of the nanostructures were observed by SEM and shown in figure 1. The as-spun nanostructures of PVAc/TiO_2, PVAc/SnO_2, and PVAc/SnO_2-TiO_2 exhibits fibers (Fig. 1a), ribbons (Fig. 1c) and ribbons (Fig. 1e) like structures and after calcination they are denoted as TNF, SNR and STNR, respectively. However, all these nanostructures are smooth and bead free. That is to say, the charges (viscoelastic force and electrostatic repulsion) between precursor solutions were successfully balanced by controlling the process parameters (humidity, flow rate, substrate rotation speed and high voltage) to suppress the influence of surface tension which drives the beads formation[35, 36].

The calcination of the as-spun nanostructures was carried out at 450 °C. The successful removal of polymeric part from TiO2/PVAc, SnO2/PVAc and SnO2-TiO2/PVAc nanostructures was first confirmed by TGA studies. The main weight loss occur between 100 to 400 °C due to the decomposition of the polymeric matrix (PVAc) and organic content of precursors present at as-spun nanostructures (Fig. SI-1[†]). Interestingly, after the calcination, the morphology of TNF (Fig. 1b) and SNR (Fig. 1d) remains unchanged, whereas PVAc/SnO_2-TiO_2 converted to fiber shaped STNF (Fig. 1f) and they are uniform throughout their lengths. The decrease in dimensions after the calcination and rougher surface is due to the loss of organic substances and crystallization during the

thermal treatment [37]. The average dimensions of the nanostructures with their standard deviation are presented (see fig. SI-2 and table SI-1†) for clear estimation. The possible mechanism for the transformation of ribbons into fibers is most likely to be 'wrapping of sheet' because of mechanical stress [38] arising during the crystallization/ dissolution. Generally when surface experiences an asymmetrical stress the excess surface energy results in wrapping or scrolling [39]. Ma et.al [40], evidenced the direct rolling of nanosheets into nanotubes of single layered titanates along the (010) axis. In single layered nanosheets, the interaction energy between atoms mostly lie in the same layer hence the sheets grows at the edges of the individual layers, rather than creating a new layer [41]. i.e the interaction energy between the atoms of inter layers was less than between in intra-layer atoms, which differs as high as 500 times. Apart from this, in the presence of asymmetrical chemical environment [39] the excess surface energy causes bending and/or curving. Therefore the gain in surface energy is sufficient to convert nanoribbons into nanofibers.

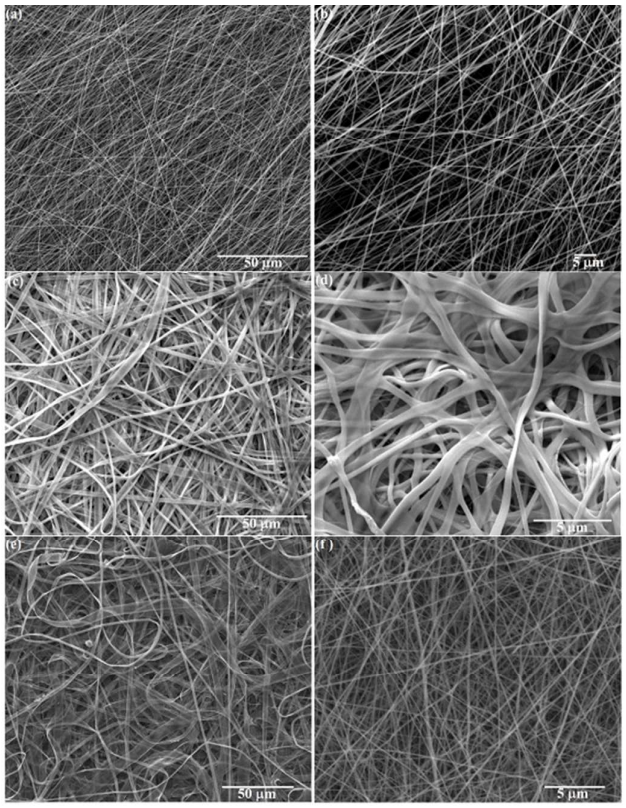

Figure 1: SEM images of as-spun nanostructures of (a) PVAc/TiO_2 (c) PVAc/SnO_2 (e) PVAc/SnO_2-TiO_2 and after calcination (b) TNF (d) SNR (f) STNF at 450 °C.

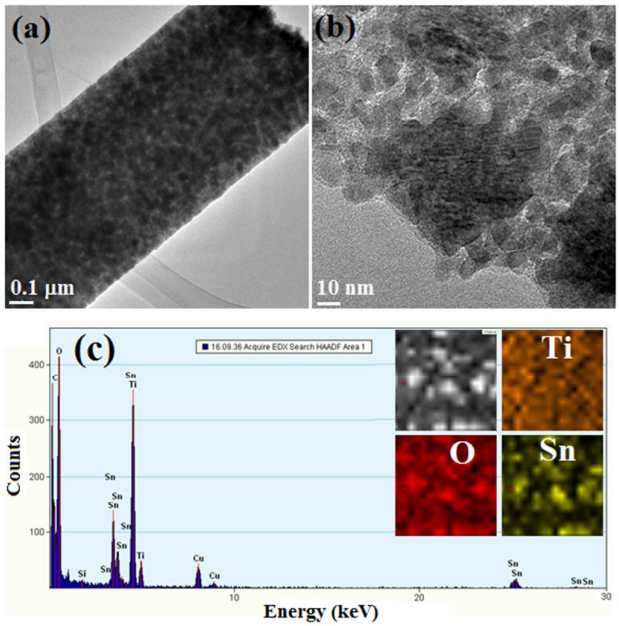

Figure-2: TEM images of (a) single nanofiber composed of STNF (b) higher magnification TEM and (c) EDX elemental mapping images of TEM micrographs for STNF.

From the TEM, presented in figure 2a it is evident that the nanostructures of STNF composed of crystalline nanoparticles along the length of the fiber. Figure 2b, at higher magnifications depicts the grains of the nanofiber. Lattice resolved image is shown in fig.SI-3† where one can identify lattice patterns of TiO_2 and SnO_2. Figure 2c, EDX spectra confirm the presence of Ti, Sn and O components in the STNF fibers. While inset of figure 2c represent the elemental mapping of TEM micrographs confirms the presence of Ti, Sn and O spatial distributions overlap in the selected region.

Crystal structure

XRD patterns of nanofibrous structures are shown in figure 3. The diffraction peaks related to TNF are indexed and confirmed to be the anatase (A) phase according to the JCPDS file no. 21-1272, as presented in figure 3a. There are no indications of the peaks related to impurities or other phases like rutile/brookite within the detection limits of XRD. The anatase phase is still predominant at 450 °C while a complete transformation was observed to occur at 750 °C from the literature [42, 43]. In case of SNR peaks are indexed according to the JCPDS file no. 72-1147 confirmed rutile SnO_2 phase which is consistent with literature [44-46]. The XRD pattern related to STNF is presented in figure 3a. It is important to note that the presence of SnO_2 hinders the growth of TiO_2 linkage which results in the formation of smaller crystallites (see table 1). This is confirmed by the broadened XRD peaks with respect to TNF and SNR. That is why there are no well resolved peaks identified in STNF. As shown in figure 3b, the corresponding peaks are identified. From figure 3b, the rutile phase ratio is higher than the SnO_2 and anatase TiO_2. The competent between the multiple phase elements might lead to dominate rutile phase in

STNF. Since both of these systems are tetragonal crystals, the lattice parameters and d-spacing values are determined by using the equation given in Ref. [47]

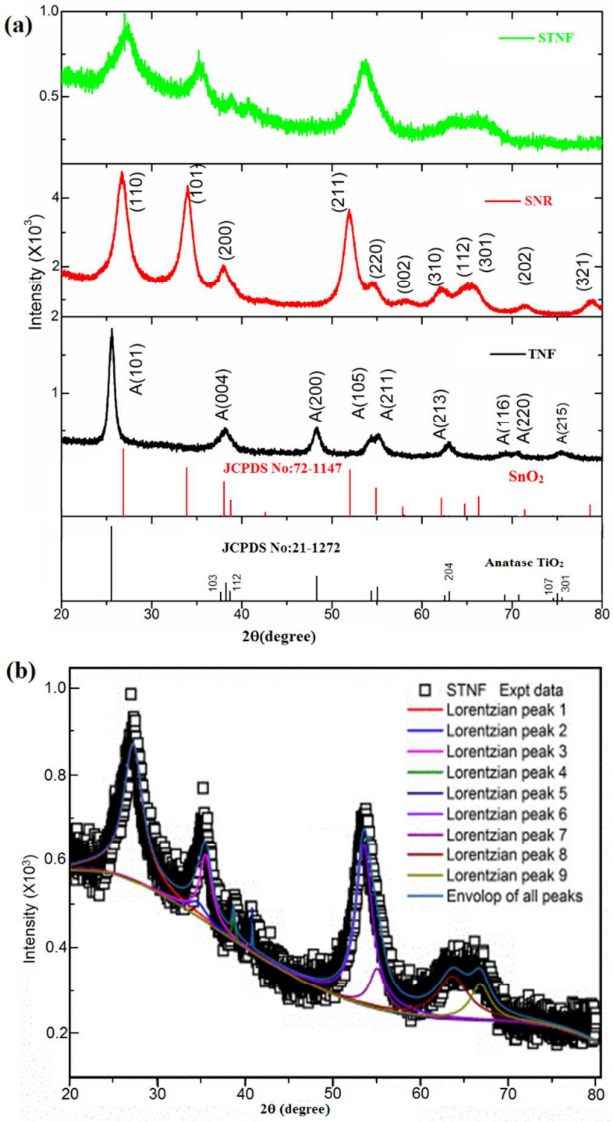

Figure 3: X-ray diffraction profiles of (a) TNF, SNR and STNF and (b) STNF decomposed using Lorentz fitting. XRD patterns are indexed according to the JCPDS no.21-1272 and JCPDS no.72-1147 for anatase TiO_2 and SnO_2 respectively.

Table 1: Lattice parameters of the TNF, SNR and STNF, where a, b, and c, are lattice parameters, V, is volume of the cell SA-Surface area; d-crystallite size

	Lattice parameters (Å)							Peak positions			
	a=b	c	c/a	$V=a^2*c$ (Å³)	V/molecule (Å³)	d (nm)	SA (m^2/g)				
TNF-A	3.7595	9.4189	2.505	133.125	33.281	11.14	135.19				
SNR	4.7208	3.1845	0.6745	70.967	35.484	7.50	214				
STNF-A								38.687 (112)	53.560 (105)		
STNF-R	4.6288	3.0189	0.6521	64.682	32.341	3.179	460.24	27.245 (110)	35.500 (101)	40.796 (111)	63.672 (301)
STNF-SnO_2	4.7157	3.0999	0.6573	68.937	34.469	3.563	231.92	34.627 (101)	55.081 (220)	66.832 (301)	

From figure 4, the full width at half maximum (FWHM) of the diffraction peaks are obtained. The FWHM values, the crystallite sizes (d_{hkl}) were calculated through Debye-Scherrer formula [48]. The calculated crystallite sizes of individual TNF, SNR and STNF are presented in the table 1. The crystallite sizes of the STNF shows smaller than the individual systems. However, by changing the calcination environment either O_2 or vacuum does not show any influence on crystalline sizes [49]. It is noted that at all Bragg reflections assigned to tetragonal phase shift to slightly higher 2θ values from STNF system. This might be due to the lattice compression/expansion during calcination. On further, the surface area (S_a) of the nanostructures are also calculated by the equation (1) [50, 51]:

$$S_a = \frac{6}{d_{hkl} * \rho} \qquad (1)$$

Where molecular density (ρ) obtained from the equation (2)

$$\rho = \frac{nM}{NV} \qquad (2)$$

Where 'n' represents the number of formula units per a unit cell (4 for anatase and 2 for SnO_2), M is the molecular weight, N is the Avogadro's number, V is the volume of the unit cell. Higher the surface area lesser the activation energy which precludes the phase transformation at below certain temperature [50].

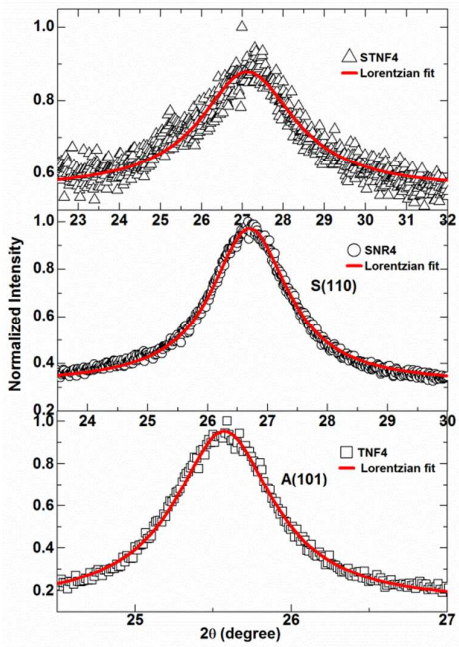

Figure 4: Line-widths of the TNF: A(101), SNR: S(110) and mixed phase STNF. The curves are fitted to Lorentz distribution.

Two types of doping *viz* (a) interstitial and (b) substitutional can be expected depending on the electronegativity and ionic radius. First one, if the electronegativity (in Pauling scale) of the Sn^{+4} is closer to Ti^{+4} and ionic radius (in Å) of Sn^{+4} is smaller than Ti^{+4}, then the lattice spacing will become larger. Then the doping will enter into the crystal cell of the oxide. While the second, if the electronegativity and ionic radius of doping metal ions match to those of the lattice metal ions in oxides, the doping metal ion will substitute itself for the lattice metal ion in the doping reactive process [52]. Since, the difference in electronegativity of Sn^{+4} (1.96) and Ti^{+4} (1.54) results the change in the volume of the STNF. It could be expected that the Sn^{+4} will replace Ti^{+4} in lattice and occupy Ti^{+4} positions by substitutional doping. Therefore, the volume of the unit cell (see table 1) of the STNF is moderately between the TNF and SNR. In addition, ionic radius of the Sn^{+4} (0.71 Å) [53] is larger than that of Ti^{+4} (0.68 Å) [53] ion, which will induce lattice distortions in STNF. From the table 1, the volume of the unit cell is very consistent, indicates that the lattice would relax as Sn^{+4} with a larger ionic radius are substituted for Ti^{+4} in TiO_2.
The lattice strain has been calculated by using Williamson-Hall (W-H) plot, by using the following equation (3)[54] :

$$\frac{\beta cos\theta}{\lambda} = \frac{1}{D} + \frac{\eta sin\theta}{\lambda} \qquad (3)$$

Where η is the strain, D is the effective crystallite size. The relation between $\beta cos\theta$ and $sin\theta$ indicates whether the sample is subjected to compressive stress or tensile strain during the thermal treatment. The plots for the samples are presented in SI (fig.SI-4[†]). Fig. SI-4, reveals that the TNF exhibits the compressive stress[55]. Whereas, SNR and STNF discloses positive slopes suggests that the both of them underwent tensile strain. The intercepts on the $\beta cos\theta$ axes give the effective crystallite sizes corresponding to zero strain[51].

UV-vis absorption

Optical absorption spectra for the nanostructures were recorded and shown in figure 5. The absorption bands of TNF exhibits peak maxima at 372 nm (3.33 eV). There are no identifications related to impurities/structural defects, possibly no absorption observed in visible region. This strong absorption peak at 372 nm is due to the band-to-band transition [56]. Ghosh et.al [14] reported that the onset and band edges were occurs at 3.17 and 3.02 eV are due to indirect transitions in rutile TiO_2, but they are not related to the occupancy of the shallow trap states. In the present study there are no sharp bands observed in SNR and STNF, in contrast with the literature[56, 57]. The synthesis methods and structural changes can affect electronic and optical properties of STNF band edge [56, 58] and effect coupling [59] between TNF and SNR system. Introduction of the SnO_2 into the TiO_2 lattice may induce changes in their light absorption properties. The STNF exhibits distinct features from the TNF and SNR, since the doping energy level of Sn^{+4} is located at 0.4 eV below the CB of the Ti^{+4}, it helps to shift in wavelength to lower regions [52, 56] in STNF. The band gap of the STNF eventually falls below the band gap of anatase TiO_2. These changes in optical band gap indicate a slight reorganization of the energy band structures [60] in the STNF, compared to pristine individual systems. Upon the introduction of SnO_2 into TiO_2, the optical absorption properties of the STNF exhibits blue shift [11, 61]. In addition, the conversion of shape (nanoribbons to nanofibers) lead to a change in fundamental absorption edge [51]. Despite the presence of SnO_2 in TiO_2, the negligible effects were also reported in the electronic propertis of TiO_2 at lower amount of guest ion introduction.

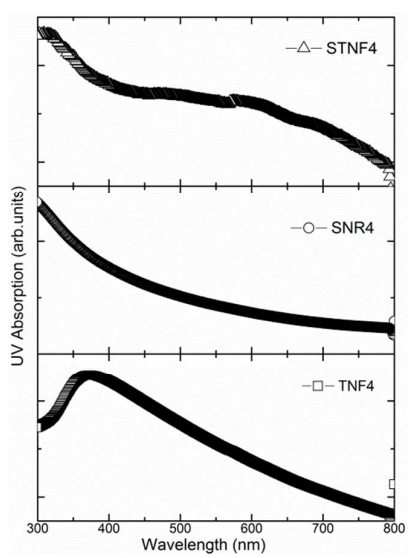

Figure 5: Optical absorption spectra for TNF, SNR and STNF nanostructures.

Photoluminescence

The room temperature PL spectra for the electrospun nanostructures were recorded at different excitation wavelengths λ_{ex1}= 325, λ_{ex2}= 330, λ_{ex3}= 350, λ_{ex4}= 397 and λ_{ex5}= 540 nm are presented (fig.SI-5†). PL spectra of TNF is shown in figure 6, but for better clarity it is plotted in two ranges as 350 to 520 nm (R_1) in figure 6a and 450 to 800 (R_2) in figure 6b. In the range R_1(λ_{ex1}, λ_{ex2}, λ_{ex3} and λ_{ex4}) four emission peaks P_1^T, P_2^T, P_3^T, and P_4^T at 383, 408, 435 and 487 nm respectively are observed. Zhu et.al [16] reported that the energy defect levels within the anatase TiO_2 nanocrystals by the optical transient infrared absorption spectroscopy method, then by considering the chemical potentials enhanced photo response was reported. The onset of absorption at P_1^T corresponds to the band gap energy of anatase TiO_2. Serpone et.al [62] reported that the band at 383 nm is assigned to highest energy indirect transition $X_{1b}\rightarrow\Gamma_3$ (where X and Γ denote the edge and center of the Brillouin zone (BZ)). The peak at P_2^T and P_3^T are ascribed to $X_{2b}\rightarrow\Gamma_{1b}$, and $X_{1a}\rightarrow\Gamma_{1b}$ respectively, which are the lowest energy allowed indirect phonon assisted transitions. The emission peak at P_4^T is assigned to shallow trap level [62]. In the range R_2 (λ_{ex1}, λ_{ex2}, λ_{ex3}, λ_{ex4} and λ_{ex5}; from Fig.6b) two emission peaks P_5^T and P_6^T at 562 nm (2.21eV) and 585 nm (2.12 eV) respectively are identified. The band in visible region at P_5^T is attributed to the radiative recombination of self-trapped excitons[63, 64]. The TNF surface exhibits emission band at P_5^T (~2.2 eV) is apparently much lower than that of the band gap energy (3.0 eV for rutile and 3.2 eV for anatase TiO_2)[16, 62]. These P_5^T and P_6^T peaks are belong to shallow traps with V_O at 0.99 eV and 1.08 eV below the CB. The shallow traps most likely concern V_O s at various energies. The green emissions can be described by the following mechanism [62].

$$TiO_2 \xrightarrow{h\nu} TiO_2(e^-/h^+) \rightarrow e_{CB}^- + h_{VB}^+ \qquad (4)$$

$$V_O^0 + e_{CB}^- \rightarrow V_O \quad (e^- \; trapping\; in\; shallow\; traps) \qquad (5)$$

$$V_O \rightarrow h_{VB}^+ \rightarrow V_O^0 + h\nu(\,Radiative\; recombnation) \qquad (6)$$

Where, V_O^0 is an ionized oxygen vacancy level composed to rapidly trap (in tens to hundreds of femtoseconds) a photogenerated CB electron which subsequently interacts with a VB hole (trapped in less than a few picoseconds) either radiatively or nonradiatively. The dominant but not exclusive route for charge carrier recombination in small semiconductor particles is the nonradiative path because of strong coupling of wave functions of trapped electrons and trapped holes with the lattice phonon.

PL emisssion spectra of SNR are shown in two ranges *viz* R_1 and R_2 in the figure 6c and 6d respectively. Four emission peaks P_1^S, P_2^S, P_3^S and P_4^S located at 372, 406, 440 and 492 nm can be seen in R_1 (Fig.6c). It is noteworthy that the bulk SnO_2 does not show luminescence, but at lower dimensions it does [65, 66]. The peak at P_1^S violet emission might be due to near band edge emission [31]. Viana et.al [13] assigned the similar peak of P_1^S to recombination of electrons from the CB to excitons bound to neutral (D^0x).

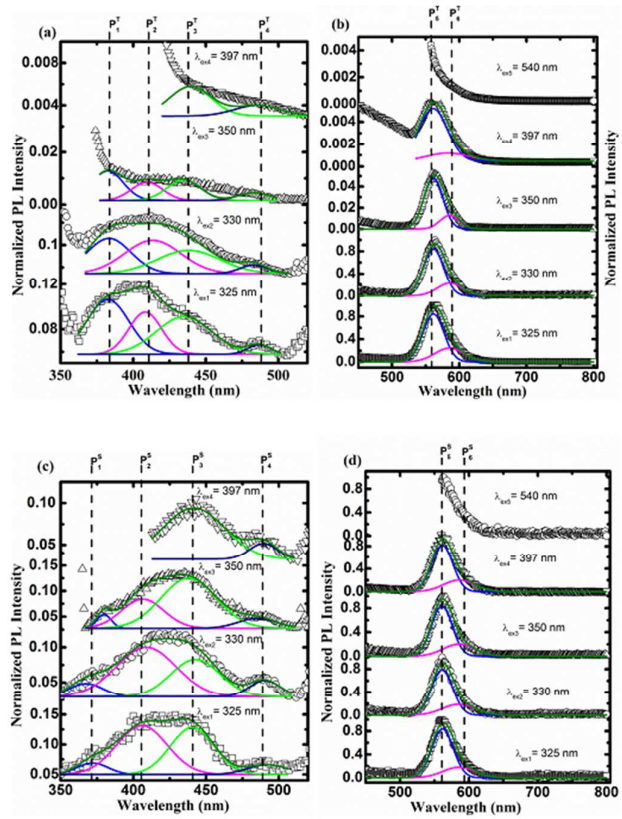

Figure 6: Normalized PL emission spectra at different excitations wavelengths of (a) TNF in the range of R_1 (b) TNF range of R_2 (c) SNR in the range of R_1 (d) SNR in the range of R_2.

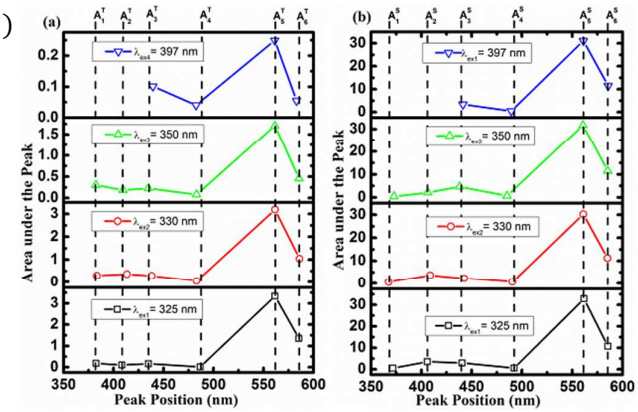

Figure 7: Area under the peaks of (a) TNF and (b) SNR at different positions.

Kim et.al.,[67] observed the peak at 416 nm (2.98 eV), but in the present studies a broad peak at P_2^S is identified. The origin of this peak is ascribed to Sn_i resulting from the nanosized SnO_2 nanoribbon like structures. The peak at P_3^S is the blue emission. Kar et.al [31] reported that the SnO_2 nanocrystals with larger sizes (26.6 nm) and nearly perfect crystalline structures exhibit

stronger violet emission. This P_3^S emission ascribed as luminescent centre due to electron transitions, mediated by defect levels in the band gap, such as V_O s and luminescent centers formed by such interstitials or dangling in presence of SnO_2 nanocrystals [45]. The peak at P_4^S which is a shallow trap level ~0.8 eV below the CB. Since the energy of the emission band is lower than the band gap energy of SnO_2 (E_g= 3.6 eV) [13, 68], the emission is not due to the direct recombination of a conduction electron in the 4p band of Sn and a hole in 2p VB of O [69]. The peak at P_4^S is assigned to isolated V_O^+ centers, which lies at higher energy than the complex V_O^+ center Ref [13]. In R_2 (see Fig 6d), a broad orange emission peaks identified as P_5^S and P_6^S positioned at 562 and 585 nm. The P_5^S peak is attributed to the radiative recombination of self-trapped excitons, while the other peak at P_6^S was also observed by Gao and Wang [70]. Both of these peaks at P_5^S and P_6^S are correspond to oxygen-deficiency defects (V_O s or Sn_i) in the SNR nanoribbons. Viana et.al [13] assigned the peak at 599 nm (2.07 eV) to V_O^+, In the present study the peak at P_6^S is observed from SNR nanoribbons is attributed to V_O^+. These midgap V_O states were defined by the broad and strong green peaks. The surface states are situated at 2.7 eV below the conduction band minimum (CBM) and 0.9 eV above the valence band maximum (VBM). The observed emission peaks (P_5^S and P_6^S from Fig.6c and 6d) 2.1 to 2.2 eV are less than the energy gap between CBM and surface states (~2.7 eV) [68]. The electrons from CB are captured by shallow trap levels below the CB and then recombine with the holes at the surface states (2.7 eV below from the CB).

The emission peak intensity with respect to the peak positions are listed (fig.SI-6 and table SI-2[†]). Higher surface area of the nanostructures higher the V_O s which results in decreased PL peak intensities. For the better comprehension the integrated area under the peak is plotted against the particular peak positions are shown in figure 7. A_1^T, A_2^T, A_3^T, A_4^T, A_5^T and A_6^T represents the area under the peaks of P_1^T, P_2^T, P_3^T, P_4^T, P_5^T, and P_6^T respectively of TNF (see Fig.7a). The area of TNF nanofibers is changed but the position of the PL peak does not change, indicating that the main PL peak is not the intrinsic feature of TiO_2. These minor changes in peak positions might be due to the non-uniform distribution of the defect levels at nanodimensions. Similarly, A_1^S, A_2^S, A_3^S, A_4^S, A_5^S, and A_6^S describes the area under the peak positions at P_1^S, P_2^S, P_3^S, P_4^S, P_5^S and P_6^S respectively of SNR is shown in figure 7b. It is noticeable from both figures (Fig.7a and Fig.7b) increased peak area at P_5^T and P_5^S which may result from the increased number of oxygen defects in TNF and SNR. The blue emission is almost zero and only red emission is observed.

Figure 8a shows the PL emission spectra of STNF, where the peak positions P_1^{ST}, P_2^{ST}, P_3^{ST}, P_4^{ST}, P_5^{ST} and P_6^{ST} at 373, 412, 433, 488, 560 and 586 nm respectively. It is also known that the PL spectra of nanostructures are usually broad and often asymmetric. The degree of crystallinity improves with the increase of calcination temperature above 400 °C. Hence the calcination temperature and tailored crystallization give rise to modified optical properties in the SNTF nanostructures. Since, STNF has the higher surface area (see table 1), V_O are easily formed in the nanofibers resulting in structural defects at Ti centres in the basic unit cell of STNF. The peaks at P_1^{ST}, P_2^{ST}, P_3^{ST} and P_4^{ST} shown little variation when compared to TNF and SNR, which is because of the SnO_2 is substitution into TiO_2 system. Interestingly, the peak positions at P_5^{ST} and P_6^{ST} is unchanged from the TNF and SNR. The origin of the green emission (540-555 nm) in bulk materials is still debatable and some authors attribute it to V_O s while other attributed it to Ti_i or Sn_i [14, 32]. However, it is widely accepted that the origin of the green emission is assigned to the recombination of electrons in the single occupied V_O s with photoexcited holes [64, 71, 72]. The area under the peaks A_1^{ST}, A_2^{ST}, A_3^{ST}, A_4^{ST}, A_5^{ST}, and A_6^{ST} positioned at P_1^{ST}, P_2^{ST}, P_3^{ST}, P_4^{ST}, P_5^{ST} and P_6^{ST} respectively of STNF is shown in figure 8b. As discussed earlier, A_5^T and A_5^S are dominant for TNF and SNR, whereas A_2^{ST} and A_4^{ST} are dominant for the STNF, i.e. the blue shift is occurred. This blue shift in peak position suggesting the increased oxygen defect states are starts forming even at lower wavelength regions.

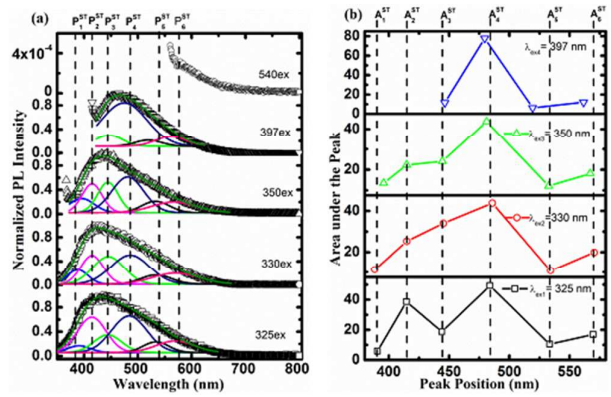

Figure 8: (a) Normalized PL emission spectra of STNF in the range of 350 to 800 nm at different excitations (λ_{ex} = 325, 330, 350, 397 and 540 nm) and (b) area under the peak for STNF.

The proposed band alignment of the nanostructures is shown in figure 9. Figure 9, exhibits six shallow energy bands in TNF and SNR. From figure 9 (TNF part), suggests that the excitations λ_{ex1}, λ_{ex2} and λ_{ex3} (3.82, 3.78 and 3.54 eV) electrons from VB would be excited to CB and populates all the six bands and recombine with holes at VB. While the excitation at λ_{ex4} (3.12 eV) the electrons will not reach even CB, so there are four bands seen near to CB. In case of λ_{ex5} (2.3 eV) excitation, the energy is 2.29 eV, hence only two bands are observed. From the figure 9 (SNR part), it is notable that the excitations at λ_{ex1} and λ_{ex2} the electron could excite more than SnO_2 band gap energy (3.6 eV) and at λ_{ex3} (3.54 eV) is close to E_g, therefore, all the six bands will be emitted. Whereas λ_{ex4} and λ_{ex5} emits only four and one band will be emitted respectively depending on their corresponding excitation energies. Band alignment of STNF is shown in figure 9, once TiO_2 and SnO_2 contact each other to form junction, band bending will occur at the interface to reach an equal Fermi level. When both of the STNF is excited, electrons transfer occurs from the CB of TiO_2 to the CB of SnO_2 and, conversely, holes transfer from the VB of SnO_2 to the VB of TiO_2. Thus the *e/h* pairs separated at the interface [73]. The band alignment for STNF as illustrated in

figure 9. Since the λ_{ex1}, λ_{ex2} and λ_{ex3} excitation energies are higher than the band gap energies of both. Therefore, the electrons from the CB of TNF to the all midgap bands of SNR would be transferred. The populated emission bands are significant at these three excitations. The excitation energy at λ_{ex4}, the electrons would be excited upto P_2^T of TNF and transfer to P_2^S, P_3^S, P_4^S, P_5^S and P_6^S bands of SNR. While at λ_{ex5} can excite upto P_5^T of TNF and transfer to P_5^S and P_6^S bands of SNR.

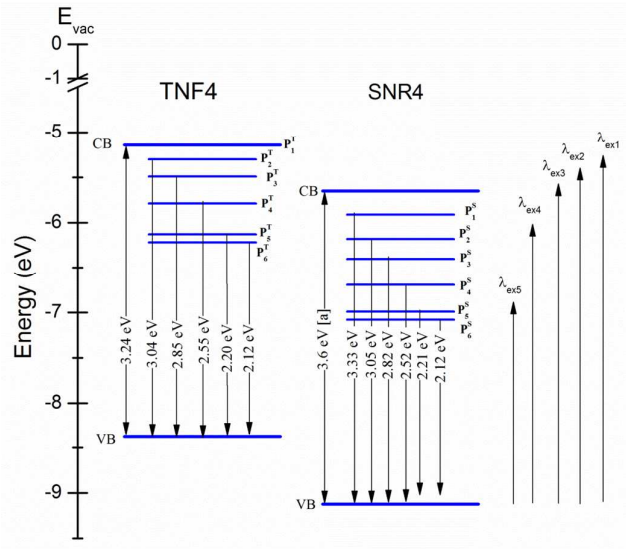

Figure 9: Band alignment with respect to vacuum energy level for STNF, where '[a]' represents the band gap of SNR is from Ref [13, 68].

Conclusions

Electrospun SnO_2 -TiO_2 nanofibers were obtained after the calcination of nanoribbon like structures. The morphologies and dimensions of the nanostructrues were observed by SEM. The possible mechanism for the transformation of ribbons into fibers was confirmed and discussed with the literature support [38]. XRD reveals that both TNF and SNR belong to tetragonal phases and the substitutional doping was confirmed. The W-H plots suggested the lattice has undergone compressive stress/tensile strain. UV-vis absorption spectra were shown band to band transition at 372 nm (3.33 eV) for TNF. In case of SNR and STNF no sharp bands were identified because of the induced structural changes from synthesis which can affect electronic and optical properties of STNF band edge [56, 58] and effect of coupling [59] between TNF and SNR system. Therefore, the optical absorption of STNF 4 exhibited blue shift. The change in morphology leads to difference in density of defects was also observed by PL spectra. The normalized PL peak exhibits six shallow trap energy levels and assigned their origin with respect to the excitation wavelength. The band bending was also expected due to the difference in electro negativity of host and substituent ions. Since, Sn substitutes for Ti. The integral peak area against the peak position shows at P_5^T and P_5^S exhibits green emission for TNF and SNR respectively, whereas STNF disclosed the blue emission at P_2^{ST} and P_4^{ST}. The proposed band alignment for the electrospun nanostructures of STNF and the possible mechanism for the defect energy bands were elaborated. Apparently, these findings would be great potential in measuring the mid-gap levels of other semiconducting nanostructures. These investigations would provide much attraction and it also requires further theoretical explanation of defect energy states in STNF system.

Acknowledgements

V.J.B. and S.V. thank The Scientific & Technological Research Council of Turkey (TUBITAK) (TUBITAK-BIDEB 2221, Fellowships for Visiting Scientists and Scientists on Sabbatical) for fellowship. T.U. thanks The Turkish Academy of Sciences–Outstanding Young Scientists Award Program (TUBA-GEBIP) for partial funding.

References

1. V. Lopez-Richard, J. C. González, F. M. Matinaga, C. Trallero-Giner, E. Ribeiro, M. R. S. Dias, L. Villegas-Lelovsky and G. E. Marques, *Nano Lett.*, 2009, **9**, 3129–3136.
2. M. C. Carotta, S. Gherardi, V. Guidi, C. Malagu', G. Martinelli, B. Vendemiati, M. Sacerdoti, G. Ghiotti, S. Morandi, A. Bismuto, P. Maddalena and A. Setaro, *Sens.Actuators B* 2008, **130**, 38-45.
3. V. J. Babu, S. R. S. Bhavatharini and S. Ramakrishna, *RSC Adv.*, 2014, **4**, 19251-19256.
4. V. J. Babu, S. Vempati, T. Uyar and S. Ramakrishna, *Phys.Chem.Phys.Chem*, 2015, **17**, 2960-2986.
5. B. Sundaray, V. J. Babu, V. Subramanian and T. S. Natarajan, *J.Eng.Fibers Fabrics*, 2008, **3**, 39-45.
6. P. G. Harrison and M. J. willett, *Nature*, 1988, **330**, 337-339.
7. R. Asahi, T. Morikawa, T. Ohwaki, K. Aoki and Y. Taga, *Science*, 2001, **293**, 269-271.
8. M. Law, H. Kind, B. Messer, F. Kim and P. Yang, *Angew.Chem.Int.Ed*, 2002, **41**, 2405-2408.
9. V. J. Babu, R. P. Rao, A. S. Nair and S. Ramakrishna, *Journal of Applied Physics*, 2011, **110**, 064327.
10. M. Radecka, K. Zakrzewska and M. Rekas, *Sens.Actuators B*, 1998, **47**, 194–204.
11. J. Lin, J. C. Yu, D. Lo and S. K. Lam, *J.Catal.*, 1999, **183**, 368-372.
12. D. O. Scanlon, C. W. Dunnill, J. Buckeridge, S. A. Shevlin, A. J. Logsdail, S. M. Woodley, C. R. A. Catlow, M. J. Powell, R. G. Palgrave, I. P. Parkin, G. W. Watson, T. W. Keal, P. Sherwood, A. Walsh and A. A. Soko, *Nat.Mater.*, 2013, **12**, 798-801.
13. E. R. Viana, J. C. González, G. M. Ribeiro and A. G. d. Oliveira, *J.Phys.Chem.C*, 2013, **117**, 7844-7849.
14. A. K. Ghosh, F. G. Wakim and R. R. Addiss.Jr, *Phys.Rev.*, 1969, **184**, 979-988.
15. F. M. Hossain, G. E. Murch, L. Sheppard and J. Nowotny, *Defect Diffus Forum* 2006, **251-252**, 1-12.
16. M. Zhu, Y. Mi, G. Zhu, D. Li, Y. Wang and Y. Weng, *J.Phys.Chem.C*, 2013, **117**, 18863–18869.
17. A. H. Kahn and A. J. Leyendecker, *Phys.Rev.*, 1964, **135**, A1321-A1325.

18. N. Daude, C. Gout and C. Jouanin, *Physical Review B*, 1977, **15**, 3229-3235.
19. X. Wang, Z. Feng, J. Shi, G. Jia, S. Shen, J. Zhou and C. Li, *Phys.Chem.Phys.Chem*, 2010, **12**, 7083−7090.
20. F. J. Knorr, D. Zhang and J. L. McHale, *Langmuir*, 2007, **23**, 8686−8690.
21. H. Ariga, T. Taniike, H. Morikawa, M. Tada, B. K. Min, K. Watanabe, Y. Matsumoto, S. Ikeda, K. Saiki and Y. Iwasawa, *J.Am.Chem.Soc.*, 2009, **131**, 14670−14672.
22. V. J. Babu, S. Vempati and S. Ramakrishna, *Rsc Adv.*, 2014, **4**, 27979-27987.
23. M. Norek, M. Michalska-Doma´nska, W. J. St¸epniowski, I. Ayala, A. Bombalska and B. Budner, *Appl.Surface Sci.*, 2013, **287**, 143-149.
24. B. Liu, C. W. Cheng, R. Chen, Z. X. Shen, H. J. Fan and H. D. Sun, *J.Phys.Chem.C*, 2010, **114**, 3407-3410.
25. J. Q. Hu, Y. Bando and D. Golberg, *Chem.Phys.Lett*, 2003, **372**, 758-762.
26. S. Luo, J. Fan, W. Liu, M. Zhang, Z. Song, C. Lin, X. Wu and P. K. Chu, *Nanotechnology*, 2006, **17**, 1695-1699.
27. S.-S. Chang, S. O. Yoon and H. J. Park, *Ceram Int*, 2005, **31**, 405-410.
28. F. Gu, S. F. Wang, C. F. Song, M. K. Lu, Y. X. Qi, G. J. Zhou, D. Xu and D. R. Yuan, *Chem.Phys.Lett*, 2003, **372**, 451-454.
29. F. Gu, S. F. Wang, M. K. Lu, X. F. Cheng, S. W. Liu, G. J. Zhou, D. Xu and D. R. Yuan, *J.Cryst.Growth*, 2004, **262**, 182-185.
30. Y.-C. Her, J.-Y. Wu, Y.-R. Lin and S.-Y. Tsai, *Appl.Phys.Lett.*, 2006, **89**, 043115.
31. A. Kar, S. Kundu and A. Patra, *J.Phys.Chem.C*, 2011, **115**, 118-124.
32. Ç. Kılıç and A. Zunger, *Phys.Rev.Lett.*, 2002, **88**, 095501.
33. V. J. Babu, M. K. Kumar, A. S. Nair, T. L. Kheng, S. I. Allakhverdiev and S. Ramakrishna, *Int.J.Hydrogen Energ*, 2012, **37**, 8897-8904.
34. V. J. Babu, A. S. Nair, P. Zhu and S. Ramakrishna, *Mater. Lett.*, 2011, **65**, 3064-3068.
35. D. Li and Y. Xia, *Adv.Mater.*, 2004, **16**, 1151–1170.
36. S. S. Lee, H. Bai, Z. Liu and D. D. Sun, *Water Research*, 2013, **47**, 4059-4073.
37. D. Li and Y. Xia, *Nano Letters*, 2003, **3**, 555-560.
38. M.-J. Paek, H.-W. Ha, T. W. Kim, S.-J. Moon, J.-O. Baeg, J.-H. Choy and S.-J. Hwang, *J.Phys.Chem.C*, 2008, **112**, 15966–15972.
39. S. Zhang, L.-M. Peng, Q. Chen, G. H. Du, G. Dawson and W. Z. Zhou, *Phys.Rev.Lett.*, 2003, **91**, 256103.
40. R. Ma, Y. Bando and T. Sasaki, *J.Phys.Chem.B*, 2004, **108**, 2115-2119.
41. D. V. Bavykin, V. N. Parmon, A. A. Lapkin and F. C. Walsh, *J. Mater. Chem.*, 2004, **14**, 3370-3377.
42. U. Balachandran and N. G. Eror, *J.Solid State Chemistry*, 1982, **42**, 276-282.
43. S. Bakardjieva, V. Stengl, L. Szatmary, J. Subrt, J. Lukac, N. Murafa, D. Niznansky, K. Cizek, J. Jirkovsky and N. Petrova, *J.Mater.Chem*, 2006, **16**, 1709-1716.
44. L. Abello, B. Bochu, A. Gaskov, S. Koudryavtseva, G. Lucazeau and M. Roumyantseva, *J. Solid State Chem.*, 1998, **135**, 78-85.
45. L. C. Nehru, V. Swaminathan and C. Sanjeeviraja, *American J. Mater.Sci.*, 2012, **2**, 6 -10.
46. K. N. Yu, Y. Xiong, Y. Liu and C. Xiong, *Phys.Rev.B*, 1997, **55**, 2666-2671.
47. B. D. Cullity, *Addison-Wesley publishing company,Inc.*, 1956, Page:42.
48. B. D. Cullity, *Addison-Wesley publishing company,Inc.*, 1956, Page :262.
49. L. Z. Liu, T. H. Li, X. L. Wu, J. C. Shen and P. K. Chu, *J.Raman Spectroscopy*, 2012, **43**, 1423–1426.
50. A. K. Tripathi, M. K. Singh, M. C. Mathpal, S. K. Mishra and A. Agarwal, *J. Alloy compd*, 2013, **549**, 114-120.
51. A. Maurya, P. Chauhan, S. K. Mishra and R. K. Srivastava, *J. Alloy compd*, 2011, **509**, 8433-8440.
52. Y. Cao, W. Yang, W. Zhang, G. Liu and P. Yue, *New J. Chem.*, 2004, **28**, 218-222
53. T. Hirata, K. Ishioka, M. Kitajima and H. Doi, *Phys.Rev.B*, 1996, **53**, 8442-8448.
54. G. K. Williamson and W. H. Hall, *Acta.Metal.*, 1953, **1**, 22-31.
55. R. R. Prabhu and M. A. Khadar, *Bull.Mater.Sci*, 2008, **31**, 511-515.
56. E. Wang, T. He, L. Zhao, Y. Chen and Y. Cao, *J. Mater. Chem.*, 2011, **21**, 144–150.
57. A. K. Sinha, P. K. Manna, M. Pradhan, C. Mondal, S. M. Yusuf and T. Pal, *RSC Adv.*, 2014, **4**, 208-211.
58. X. Xu, G. Yang, J. Liang, S. Ding, C. Tang, H. Yang, W. Yan, G. Yang and D. Yu, *J. Mater. Chem. A*, 2014, **2**, 116–122.
59. P. Du, L. Song, J. Xiong, N. Li, Z. Xi, L. Wang, D. Jin, S. Guo and Y. Yuan, *Electrochim.Acta*, 2012, **78**, 392-397.
60. J. Zhang, W. Peng, Z. Chen, H. Chen and L. Han, *J. Mater. Chem.A*, 2013, **1**, 8453-8463
61. S. K. Zheng, T. M. Wang, W. C. Hao and R. Shen, *Vacuum*, 2002, **65**, 155-159.
62. N. Serpone, D. Lawless and R. Khairutdinov, *J.Phys.Chem.*, 1995, **99**, 16646-16654
63. P. J. Young, C. Sun-Woo, A. Kandasami and K. S. Sub, *J.Nanosci.Nanotechnol.*, 2010, **10**, 3604-3608.
64. H. Tang, H. Berger, P. E. Schmid and F. Lévy, *Solid State Commun*, 1993, **87**, 847–850.
65. X. Wu, B. Zou, J. Xu, B. Yut, G. Tang, G. Zhangf and W. Chen, *Nanostructured mater.*, 1997, **8**, 179-189.
66. J. Hu, Y. Bando, Q. Liu and D. Golberg, *Adv.Funct.Mater.*, 2003, **13**, 493-496.
67. T. W. Kim, D. U. Lee and Y. S. Yoon, *J. Appl.Phys.*, 2000, **88**, 3759.
68. X. T. Zhou, F. Heigl, M. W. Murphy, T. K. Sham, T. Regier, I. Coulthard and R. I. R. Blyth, *Appl.Phys.Lett.*, 2006, **89**, 213109.
69. M. H. Harunsani, F. E. Oropeza, R. G. Palgrave and R. G. Egdell, *Chem. Mater.* , 2010, **22**, 1551–1558.
70. T. Gao and T. Wang, *Mater.Res.Bull.*, 2008, **43**, 836-842.
71. J. H. He, T. H. Wu, C. L. Hsin, K. M. Li, L. J. Chen, Y. L. Chueh, L. J. Chou and Z. L. Wang, *Small*, 2006, **2**, 116-120.
72. X. Xiang, X. T. Zu, S. Zhu, L. M. Wang, V. Shutthanandan, P. Nachimuthu and Y. Zhang, *J.Phys.D:Appl.Phys.*, 2008, **41**, 225102.
73. H. Shi, M. Zhou, D. Song, X. Pan, J. Fu, J. Zhou, S. Ma and T. Wang, *Ceram Int*, 2014, **40**, 10383-10393.